International Journal of Solids and Structures 46 (2009) 3257–3271

Contents lists available at ScienceDirect

International Journal of Solids and Structures

journal homepage: www.elsevier.com/locate/ijsolstr

Analysis of structure and strain at the meso-scale in 2D granular materials

Ngoc-Son Nguyen *, Hélène Magoariec, Bernard Cambou, Alexandre Danescu

LTDS – UMR 5513, Ecole Centrale de Lyon, 36 av. Guy de Collongue, Ecully 69134 Cedex, France

ARTICLE INFO

Article history:
Received 17 February 2009
Received in revised form 8 April 2009
Available online 3 May 2009

Keywords:
Granular material
Meso-scale
Strain
Structure

ABSTRACT

In this paper, we introduce a new scale called *the meso-scale* in order to define an appropriate local scale for multi-scale kinematic analysis in granular materials. The proposed meso-scale corresponds to sub-domains obtained by subdividing a 2D granular assembly taking into account load-bearing contacts. For each sub-domain, a strain tensor is defined and a description of its structure is proposed. Our analysis, carried out on a biaxial compression test, reveals that strain is significantly related to the structure at the meso-scale: (1) strain in the major (respectively, minor) principal compression direction is largest within the sub-domains which are elongated in the minor (respectively, major) principal compression direction, and (2) contractancy takes place within the sub-domains which are elongated in the minor principal compression direction whereas dilatancy takes place within the sub-domains which are elongated in the major principal compression direction. Furthermore, we emphasize a relation between strain at the meso-scale and the induced anisotropy of granular materials during deviatoric loading.

1. Introduction

The multi-scale approach has long been investigated for the macroscopic modeling of granular materials. Two scales are usually distinguished: the macro-scale corresponding to the statistically representative volume element level, and the micro-scale, defined at the particle level (contacts between particles, for example). However, working at the particle level introduces some difficulties in defining the strain in a granular assembly from a micromechanical point of view. In fact, the microscopic kinematic variables (particle translation, particle rotation) are discrete, whereas strain is a concept used for a continuum medium. Consequently, the change of scale for kinematic variables in granular materials is a complex problem. One way to overcome this difficulty is to introduce an intermediate scale between the macro-scale and the micro-scale, at which strain can be defined using the tools of continuum mechanics.

The definition of strain based on the equivalent continuum approaches proposed by Bagi (1996), Kruyt and Rothenburg (1996), Kuhn (1997, 1999), Cambou et al. (2000), and Dedecker et al. (2000), gives a good approximation of macroscopic strain from particle displacement. The granular sample is subdivided into sub-domains assumed to be continuous, where a local strain field is defined. The difference between these approaches lies in the partition of a granular assembly. Kuhn (1997, 1999, 2003) used the partition proposed by Satake (1992) that subdivides a 2D granular assembly into polygonal sub-domains called *void-cells* whose edges connect the centers of particles in contact. In this framework, Kuhn modified the partition so that it includes only the particles which are part of the load-bearing framework. By measuring the deformation at the void-cell scale, the author found out that strain is very non-uniform at this scale. This is why the proposed approach uses multi-scale analysis to capture this non-uniform nature. Moreover, an interesting feature of this non-uniformity is that it is not random or disordered but quite structured.

The aim of this paper is to further investigate the structured nature of strain at the void-cell scale in 2D granular assemblies, on the basis of Kuhn's approach, by using the Discrete Element Method (DEM). The void-cell scale is defined as the meso-scale in our approach. First of all, the aforementioned partition will be constructed for a 2D assembly of disks. Next, the structure at the defined meso-scale (mesoscopic structure) is characterized and its evolution during a biaxial compression test is investigated. The strain at the meso-scale (mesoscopic strain) is then defined. Finally, we focus on the relation between the strain and the structure at the meso-scale, on the link between the particle translation, and the mesoscopic strain and on the role of the induced anisotropy of a granular material in the mesoscopic strain during the biaxial compression process.

2. Numerical biaxial test

2.1. Description of the biaxial test

The investigation needs local information at the particle level. To this end, we performed a numerical simulation of a biaxial compression test using the PFC2D (2D Particle Flow Code) software.

* Corresponding author.
E-mail address: ngoc-son.nguyen@ec-lyon.fr (N.-S. Nguyen).

0020-7683/$ - see front matter © 2009 Elsevier Ltd. All rights reserved.
doi:10.1016/j.ijsolstr.2009.04.019

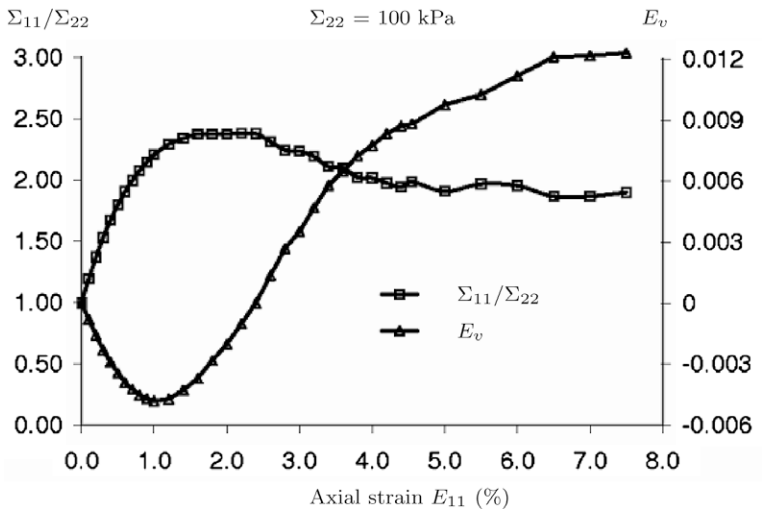

Fig. 1. Macroscopic stress ratio Σ_{11}/Σ_{22}–axial strain E_{11} relationship and macroscopic volumetric behavior E_v of the analyzed assembly during biaxial compression.

The PFC2D software is developed and licensed by HCItasca, which is widely used to model the movement and interaction of circular particles by using the Discrete Element Model (DEM). The DEM was introduced by Cundall (1971) to analyze rock mechanics problems and then applied to soil mechanics problems by Cundall and Strack (1979). This software is distinguished by its assumption that particles are rigid but that there is some slight overlap at contacts. The contact force can be derived from the magnitude of the overlap between particles via a force–displacement law. However, this overlap must be small enough with respect to particle size. The computation strategy of PFC2D is a time stepping algorithm that consists in repeating the application of the motion law to each particle and the force–displacement law to each contact.

The analyzed granular assembly is composed of 25,000 randomly generated disks in a rectangular box made up of four rigid frictionless walls. The diameter of disks is uniformly distributed from 4.7×10^{-3} m to 9.4×10^{-3} m. The local contact law is linear elastic with friction: the intergranular friction angle equal to 30° and the imposed normal and tangential local stiffnesses equal to 5.0×10^7 N/m. The initial sample size is: $h_1 = 1.35$ m in the major principal compression direction denoted (1), $h_2 = 0.9$ m in the minor principal compression direction denoted (2), and $h_3 = 1.0$ m the thickness of the assembly in the direction denoted (3) perpendicular to the considered plane (1,2). In this paper, directions (1) and (2) correspond to the vertical and horizontal directions, respectively.

The sample is compacted by gradually increasing the size of all disks until an isotropic stress state of $\Sigma_{11} = \Sigma_{22} = 100$ kPa is attained. At the end of the compacting phase, the porosity is close to 0.16, the coordination number is close to 3.8, and the obtained initial state is isotropic. The sample is then subjected to a biaxial compression test by prescribing an axial strain rate $\dot{E}_{11} = -10^{-2}$ s^{-1} on the upper and lower walls while keeping a constant pressure $\Sigma_{22} = 100$ kPa on the lateral walls. The axial strain is increased in small increments of more or less $\delta E_{11} \simeq -2 \times 10^{-4}$.

The macroscopic behavior of the tested granular assembly is illustrated in Fig. 1. It is representative of the behavior of a medium dense granular material which undergoes a contractancy phase early and until an axial strain of about 1.0%, and then followed by a dilatancy phase. The peak of stress is reached at an axial strain of about 2.0% and then followed by a softening phase.

Fig. 2 illustrates the evolution of the ratio between the diagonal components H_{11} and H_{22} of the contact fabric tensor $\boldsymbol{H} = \langle \boldsymbol{n}^c \otimes \boldsymbol{n}^c \rangle$ (here $\boldsymbol{n}^c$ is the unit contact normal vector and the operator $\langle \cdot \rangle$ means average over the sample) and the evolution of the coordination number N_c of the analyzed assembly during loading. The contact distributions at the initial and peak states are represented by polar diagrams in Fig. 3 in which the number of contacts $N^c(\theta)$ oriented in a given polar angle interval is plotted.

2.2. Choice of behavior zones to analyze

In order to evaluate the heterogeneity level of the particle center displacement field with respect to the corresponding displacement field of an equivalent homogeneous continuum, we define a quantity called *displacement non-uniformity ratio* $\varrho^p_{\delta u}$ for each particle p in the assembly as follows:

$$\varrho^p_{\delta u} = \frac{|\delta \boldsymbol{u}^p - \delta \boldsymbol{\zeta}^p|}{|\delta \boldsymbol{\zeta}|_{\max}} \tag{1}$$

where $|\cdot|$ means the norm of a vector ($|\boldsymbol{a}| = \sqrt{a_i a_i}$). $\delta \boldsymbol{u}^p$, $\delta \boldsymbol{\zeta}^p$ are the displacements of the center of particle p, corresponding to the discrete medium and the equivalent homogeneous continuum, respectively. $|\delta \boldsymbol{\zeta}|_{\max}$ is the maximal norm of the displacement field of the latter.

We plot, in Fig. 4, all particles in the assembly at different strain increments: (a) and (b) for the zone before the peak, (c) for the zone just before the peak, and (d) for the zone after the peak. The color[1] of each particle corresponds to the value of $\varrho^p_{\delta u}$ displayed on the color map. It can be seen that the discrete displacement field remains rather *homogeneous* at the first two strain increments considered in this figure but it becomes very heterogeneous at the last two ones. This result highlights the appearance of shear bands inside the assembly in the zones just before and after the peak of the stress–strain curve. The appearance of shear bands inside granular materials during deviatoric loading has been experimentally confirmed by numerous authors in the literature (Yoshida et al., 1994; Oda and Kazama, 1998).

The analysis presented in this paper is statistically treated for whole granular assembly using averaging operations. Therefore, it is crucial that the deformation is not localized inside shear bands. We thus chose to carry out our analysis on the behavior zone before the peak of the stress–strain curve, mainly for the

[1] For interpretation of the references to color in Fig. 4, the reader is referred to the web version of this paper.

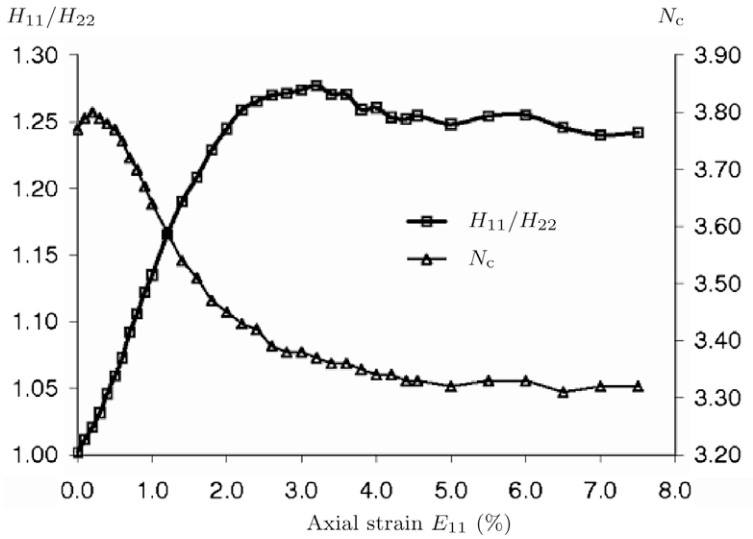

Fig. 2. Evolution of the ratio H_{11}/H_{22} of the contact fabric tensor and of the coordination number N_c of the analyzed assembly during biaxial compression.

two strain increments (a) $E_{11} = [0.2\%, 0.22\%]$ and (b) $E_{11} = [1.2\%, 1.22\%]$.

3. A meso-scale for kinematic analysis

3.1. Choice of an appropriate meso-scale

The geometric structure of a 2D granular assembly can be described by a particle graph which entirely subdivides the assembly into polygonal sub-domains (Satake, 1992). In this paper, sub-domains are similar to the void-cells considered in the framework of Kuhn (1997, 1999) which are surrounded by the branches connecting two centers of particles participating in the load-bearing. The particle graph is updated during loading. The particles which do not participate in supporting the external loading (isolated particles) are not taken into account in the particle graph. Although such isolated particles are not taken into account in a *given* particle graph, they may participate in the load-bearing in the next stages of loading and can thus be taken into account in *further updated* particle graphs.

We propose the following procedure to obtain such a particle graph: using the Delaunay triangulation method (Lee and Schachter, 1980; Guibas et al., 1990), an assembly of particles is subdivided into triangles such that each triangle connects three particle centers. A branch in the Delaunay network can be defined either as a *contact branch* if two connected particles are in contact or as an *open branch* if otherwise. If neighbouring triangles sharing an open branch are associated, the whole granular sample is replaced by a covering of polygonal sub-domains, each of which is formed by associated triangles. Therefore, each sub-domain is surrounded by branches connecting two centers of particles in contact. In order to avoid the wall-effect on the result of our analysis, we do not take into account the *border sub-domains* which contain any particle in contact with walls.

Fig. 5 shows particles and sub-domains of the particle graph obtained with the above considered granular assembly at the initial state. The number of edges of sub-domains varies widely from 3 to 10 with a mean value equal to around 4. The composition of the particle graph in terms of percentage by number of sub-domains versus their number of edges is shown in Fig. 6. It can be seen that the triangles and quadrangles occupy more than 70% of the total number of sub-domains in the particle graph.

In this paper, the considered *meso-scale* corresponds to the sub-domain level in the constructed particle graph. At this scale, the internal heterogeneity of a granular sample in terms of structure

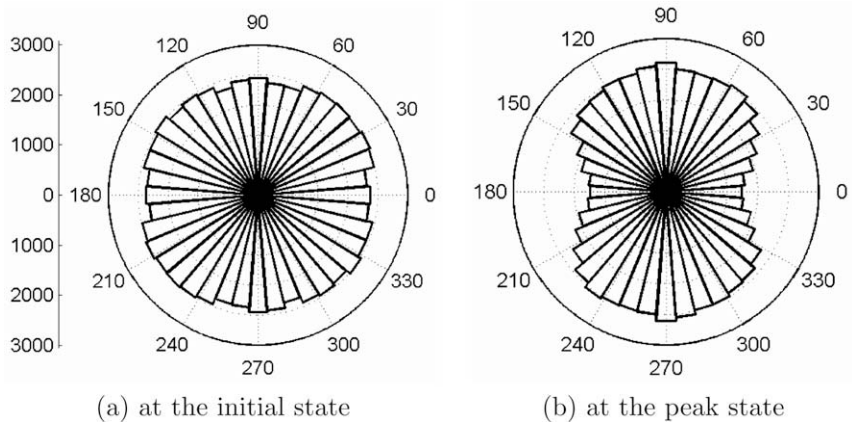

Fig. 3. Contact distributions $N^c(\theta)$ at the initial and peak states.

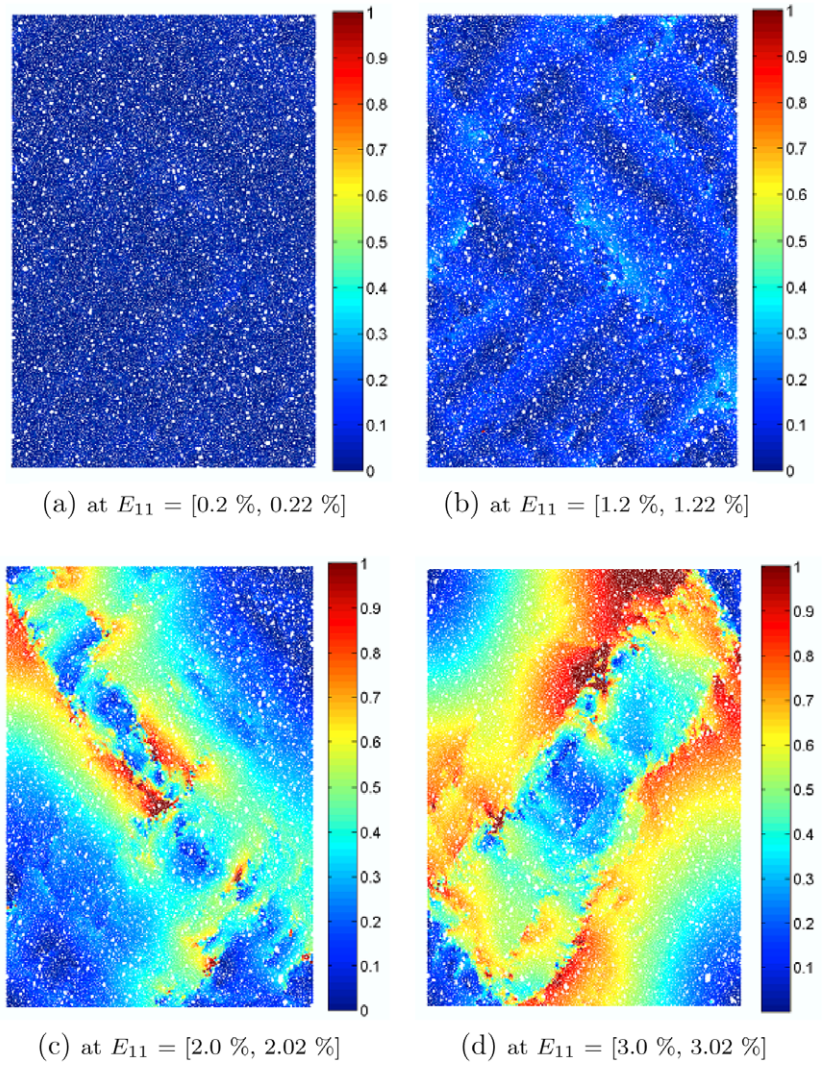

Fig. 4. Heterogeneity of the particle center displacement field at different strain increments.

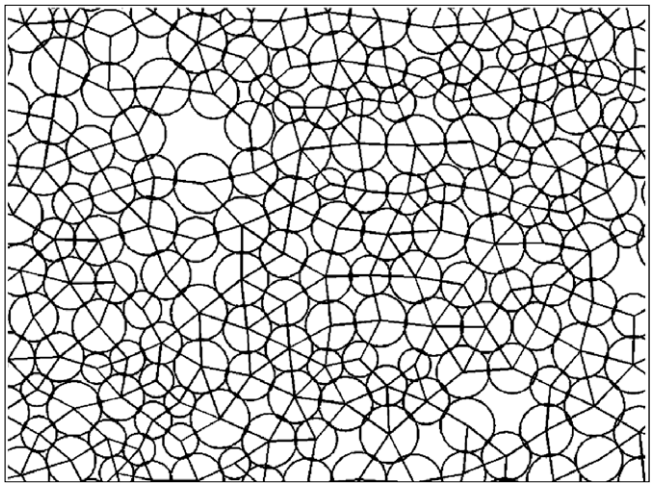

Fig. 5. A close-up of the granular assembly and the associated particle graph at the initial state.

(porosity, geometry) can be easily described. We show later that this heterogeneity plays an important role in deformation at the meso-scale.

3.2. Structure at the meso-scale

3.2.1. Characterization of the mesoscopic structure

A macroscopic description of a granular material accounting for information at the particle level needs to define two kinds of variable: a first set of variables characterizing the density of the assembly (porosity, coordination number, etc.) and a second one characterizing its geometry (fabric tensor, etc.). We define here the same kinds of variable at the meso-scale to describe the structure of each sub-domain.

3.2.1.1. Variables characterizing density at the meso-scale. The density of a sub-domain is described by either porosity, ϕ^h, defined as the ratio between the voids area inside the sub-domain and the area delimited by its edges, or a quantity called *valence*, r^h, defined as the number of its edges. Sub-domain valence r^h appears to be a physically meaningful variable to describe the density of a sub-domain because it is related to the number of load-bearing contacts of the sub-domain. Concerning the porosity of a sub-domain, it can be computed for two cases: ϕ_1^h for a first case where the isolated particles are deleted from the particle graph, and ϕ_2^h for a second one where the isolated particles are kept. The porosity of the overall particle assembly for the first case ($\langle\phi_1^h\rangle_v = 0.19$, subscript v means a volume-weighted average) is, of course, signif-

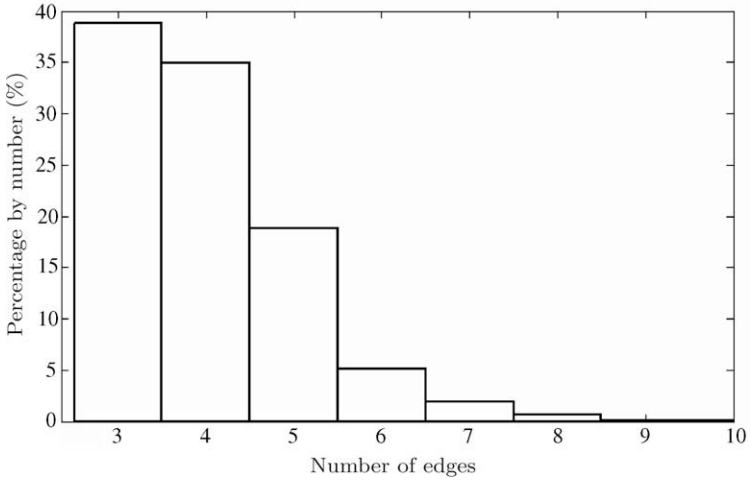

Fig. 6. Percentage by number of sub-domains versus their number of edges at the initial state.

icantly higher than that for the second one ($\langle\phi_2^h\rangle_v = 0.16$). Fig. 7 points out the correlations between sub-domain valence r^h and sub-domain porosities ϕ_1^h, ϕ_2^h. These are correlations in a statistical sense, in which the volume-weighted mean porosity is taken over all sub-domains having a given valence. The correlation for the first case is very clear: the triangles, quadrangles and pentagons tend to occupy dense zones whereas sub-domains having a higher valence occupy looser zones in the assembly. However, sub-domain valence r^h is weakly correlated to sub-domain porosity ϕ_2^h for the second case. Thus, *sub-domain valence* r^h *and sub-domain porosity* ϕ_1^h computed with the elimination of isolated particles from the proposed particle graph seem to be appropriate variables to describe density at the meso-scale of a granular material. Hereafter, our analysis is carried out on sub-domains without isolated particles.

3.2.1.2. Variables characterizing geometry at the meso-scale. The geometry of a sub-domain is described by a *loop tensor* which is analogous to the loop tensor proposed by Tsuchikura and Satake (1998).

$$\boldsymbol{L}^h = \sum_{k=1}^{r^h} l^k \boldsymbol{n}^k \otimes \boldsymbol{n}^k \tag{2}$$

where l^k, $\boldsymbol{n}^k$ are the length and the unit branch vector, respectively, of branch k of sub-domain h. We modify the loop tensor of Tsuchikura and Satake in such a way that the trace of the loop tensor $\boldsymbol{L}^h$ gives the perimeter of sub-domains.

The loop tensor is then decomposed into an isotropic part roughly describing the size of a sub-domain and a deviatoric part describing its shape:

$$\boldsymbol{L}^h = \frac{1}{2}\alpha^h \boldsymbol{I} + \boldsymbol{D}^h \tag{3}$$

$$\alpha^h = tr(\boldsymbol{L}^h) = \sum_{k=1}^{r^h} l^k \tag{4}$$

where $\boldsymbol{I}$ is the unit tensor, $\boldsymbol{D}^h$ is the deviatoric part. Two key geometrical quantities of a sub-domain are derived from the loop tensor $\boldsymbol{L}^h$:

(1) The dimensionless elongation degree β^h:

$$\beta^h = \frac{\sqrt{\boldsymbol{D}^h : \boldsymbol{D}^h}}{\alpha^h} \tag{5}$$

(2) The elongation direction, $\boldsymbol{m}^h$, corresponding to a unit vector in the major principal direction of $\boldsymbol{L}^h$. We chose to define the orientation of a sub-domain with respect to the horizontal direction as that of its elongation direction. The sub-domain orientation angle, θ^h, is then derived from $\boldsymbol{m}^h = (\cos(\theta^h), \sin(\theta^h))$.

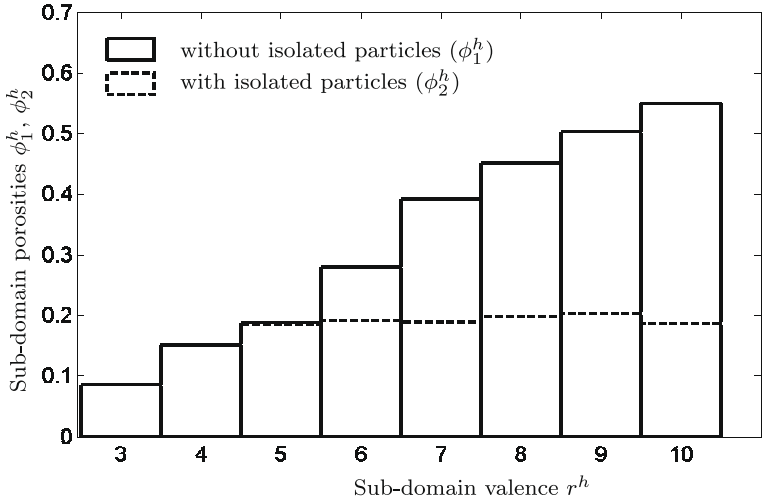

Fig. 7. Correlation between sub-domain valence r^h and sub-domain porosities ϕ_1^h, ϕ_2^h at the initial state.

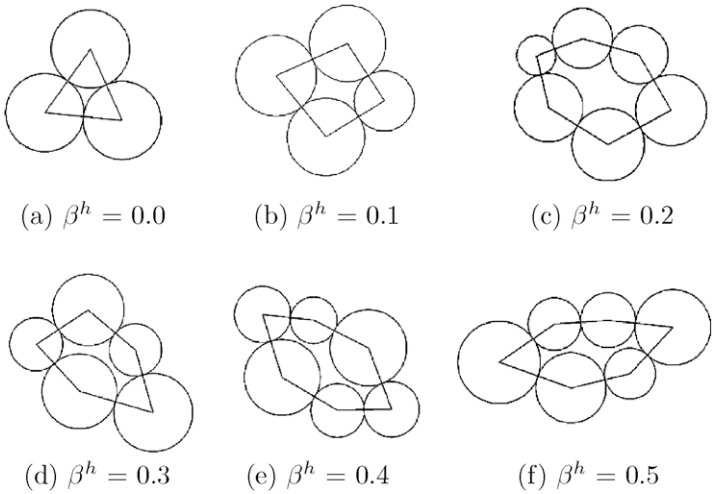

Fig. 8. Sub-domains with different elongation degrees β^h.

The elongation direction of a sub-domain corresponds approximately to the direction in which the contacts of this sub-domain are preferentially oriented. The tendency of preferential contact orientation in the elongation direction of a sub-domain increases with the elongation degree. The significance of sub-domain elongation degree β^h is illustrated in Fig. 8, in which six sub-domains correspond to six increasing values of β^h: 0.0, 0.1, 0.2, 0.3, 0.4, and 0.5, respectively. It should be noted that a sub-domain of regular shape have zero elongation degree β^h and, in this case, there is no elongation direction $\boldsymbol{m}^h$ for this sub-domain. Therefore, the role of elongation direction $\boldsymbol{m}^h$ have to be combined with the value of elongation degree β^h.

Fig. 9 shows the distribution of sub-domain elongation degree β^h in the particle graph at the initial state. We can see that the heterogeneity in terms of sub-domain elongation degree β^h is significant. The value of the elongation degree varies widely from a minimum value $\beta^h_{\min}$ equal to 0.0 to a maximum value $\beta^h_{\max}$ equal to 0.5 with a volume-weighted mean value $\langle\beta^h\rangle_v$ equal to 0.2.

In order to analyze the role of sub-domain elongation degree β^h and of sub-domain orientation θ^h, we chose to define six types of sub-domain related to varying values of β^h and θ^h. To this end, we first define two *elongation classes*: *W* and *S*, i.e. *weakly* and *strongly* elongated sub-domains, respectively, considering the value of $\langle\beta^h\rangle_v$ as a threshold between the two classes. For each of these two elongation classes, we then define three *orientation sub-classes*: *V*, *O*, and *H*, i.e. sub-domains oriented *vertically* (in the *major* principal compression direction), *obliquely*, and *horizontally* (in the *minor* principal compression direction), respectively, depending on the value of sub-domain orientation θ^h. This finally leads to six types of sub-domain to be analyzed: *WV*, *WO*, *WH*, *SV*, *SO*, and *SH* as shown in Table 1.

Fig. 10 shows the composition in terms of the percentage by number of sub-domains belonging to each elongation class with respect to the total number of sub-domains in the particle graph at the initial state. We can see that the class of weakly elongated sub-domains contains an high proportion of triangles whereas the class of strongly elongated sub-domains contains an high proportion of quadrangles and pentagons.

3.2.2. Evolution of the mesoscopic structure

A well-known consequence of prescribing deviatoric loading on a granular material whose nature is discrete is the induced anisotropy in terms of contact distribution. This induced anisotropy leads to a modification of the particle graph during loading. Here, we

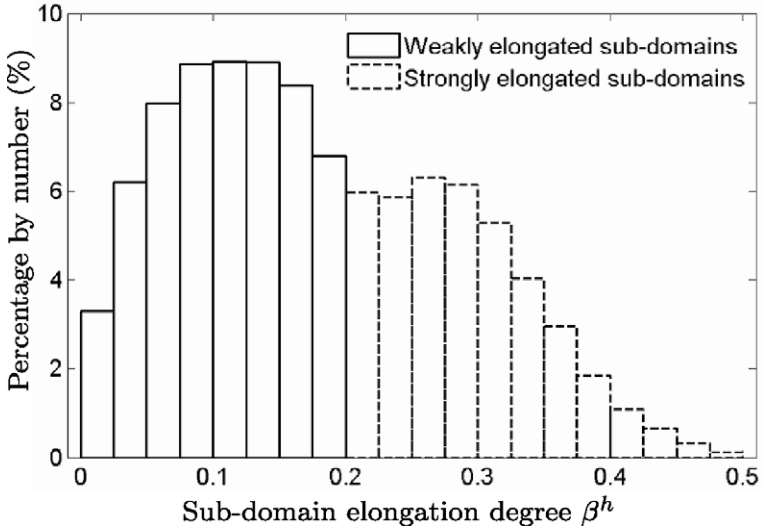

Fig. 9. Distribution of sub-domain elongation degree β^h at the initial state.

Table 1
Classification of sub-domains into two elongation classes (*W* and *S*) and three orientation sub-classes (*V*, *O*, and *H*) leading to six types of sub-domain (*WV*, *VO*, *WH*, *SV*, *SO*, *SH*).

Elongation classes	Types of sub-domain	Elongation degree β^h	Orientation angle θ^h
W	*WV*	$[\beta^h_{\min}, \langle\beta^h\rangle_v]$	$[\pi/3, 2\pi/3]$
	WO		$[\pi/6, \pi/3] \cup [2\pi/3, 5\pi/6]$
	WH		$[0, \pi/6] \cup [5\pi/6, \pi]$
S	*SV*	$[\langle\beta^h\rangle_v, \beta^h_{\max}]$	$[\pi/3, 2\pi/3]$
	SO		$[\pi/6, \pi/3] \cup [2\pi/3, 5\pi/6]$
	SH		$[0, \pi/6] \cup [5\pi/6, \pi]$

investigate how the particle graph evolves during the biaxial compression test.

The distribution of sub-domains belonging to each elongation class is qualitatively shown in Fig. 11 in the form of polar diagrams representing the number of sub-domains $N^h(\theta)$ oriented in a given polar angle interval. We note that at the initial state, where the granular material is isotropic, sub-domains in the particle graph are isotropically oriented whatever sub-domain elongation degree β^h. During loading, sub-domains tend to be preferentially oriented in the major principal compression direction. It is interesting to note that the preferential direction of sub-domain distribution coincides with that of contact distribution. Furthermore, the tendency of preferential sub-domain distribution in the major principal compression direction is closely related to sub-domain elongation degree β^h: the distribution of the strongly elongated sub-domains is much more anisotropic than that of the weakly elongated sub-domains.

In order to quantify the anisotropy in terms of sub-domain distribution in the particle graph, we define a *texture tensor* $\boldsymbol{T}$ as follows:

$$\boldsymbol{T} = \frac{1}{N}\sum_{h=1}^{N} \boldsymbol{m}^h \otimes \boldsymbol{m}^h \tag{6}$$

where N is the total number of sub-domains and $\boldsymbol{m}^h$ is the elongation direction of the sub-domain h.

Texture tensor $\boldsymbol{T}$ is then computed for each elongation class. In the following, $\boldsymbol{T}^W$ and $\boldsymbol{T}^S$ denote the texture tensors for the classes of weakly and strongly elongated sub-domains, respectively. The evolutions of $\boldsymbol{T}$, $\boldsymbol{T}^W$ and $\boldsymbol{T}^S$ during loading are shown in Fig. 12. It can be noted that all these three texture tensors are nearly diagonal, which means that the principal directions of sub-domain distribution coincide with the principal compression directions. These three texture tensors are almost isotropic at the initial state, but they become more and more anisotropic during loading with an increase of the T_{11}, T^W_{11}, T^S_{11} components and a decrease of the T_{22}, T^W_{22}, T^S_{22} components. More precisely, the evolution of $\boldsymbol{T}^S$ is much stronger than that of $\boldsymbol{T}^W$, which quantitatively confirms the polar diagrams in Fig. 11 and emphasizes the ability of the texture tensors to quantify the anisotropy in terms of sub-domain distribution.

The structural evolution of the particle graph has also been investigated by Tsuchikura and Satake (1998) and Kuhn (1999). Kuhn underlined the fact that the preferential sub-domain distribution in the major principal compression direction is related to both the creation and the loss of contacts in the major and minor principal compression directions, respectively. Fig. 13 illustrates the formation of two new sub-domains oriented in the major principal compression direction at the peak state. These new sub-domains are formed by the creation and the loss of contacts oriented in the major and minor principal compression direction, respectively, with reference to the particle configuration at the initial state.

Tables 2 and 3 point out some characteristics of the six types of sub-domain at the initial and peak states. Mean valence, $\langle r^h\rangle$, and mean porosity, $\langle\phi^h_1\rangle_v$, of these types of sub-domain do not depend on sub-domain orientation θ^h at the initial state, but they depend significantly on the latter at the peak state: those of type *SV* (respectively, *WV*) are higher than those of types *SO*, *SH* (respectively, *WO*, *WH*). In general, mean porosity $\langle\phi^h_1\rangle_v$ of the sub-domains oriented in the major principal compression direction increases while that of sub-domains oriented obliquely and in the minor principal compression direction decreases. However, sub-domain elongation degree β^h does not depend significantly on sub-domain orientation θ^h and it does not increase significantly during loading. It should be noted that the mean porosity $\langle\phi^h_1\rangle_v$ of the strongly elongated sub-domains is lower than that of the weakly elongated sub-domains, although the mean valence of the former is higher than that of the latter. This result can be explained by the fact that porosity ϕ^h_1 of a sub-domain decreases when its elongation degree β^h increases.

3.3. Strain tensor at the meso-scale

The strain within each sub-domain is computed by using the definition of Kuhn (1997, 1999). This definition is based on the equivalent continuum approach for which each sub-domain is replaced by a continuous volume defined by nodes corresponding to particle centers. A suitable translation field is then assigned to

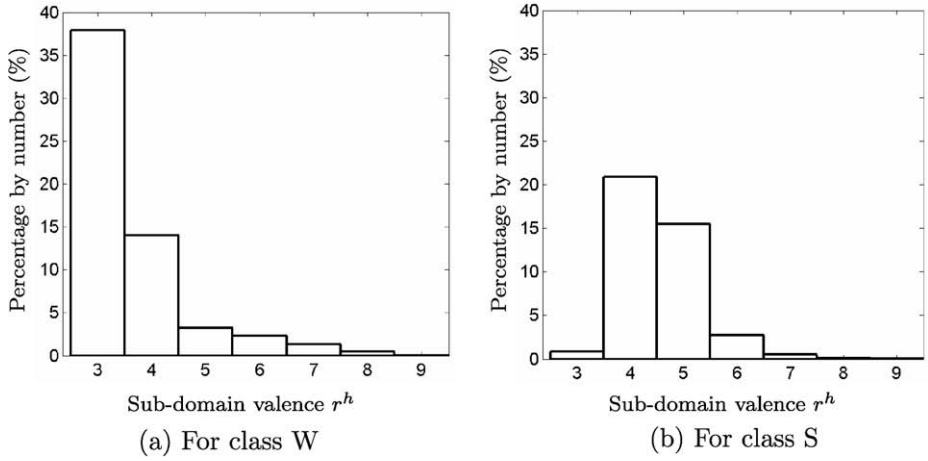

Fig. 10. Composition of two elongation classes *W* and *S* at the initial state.

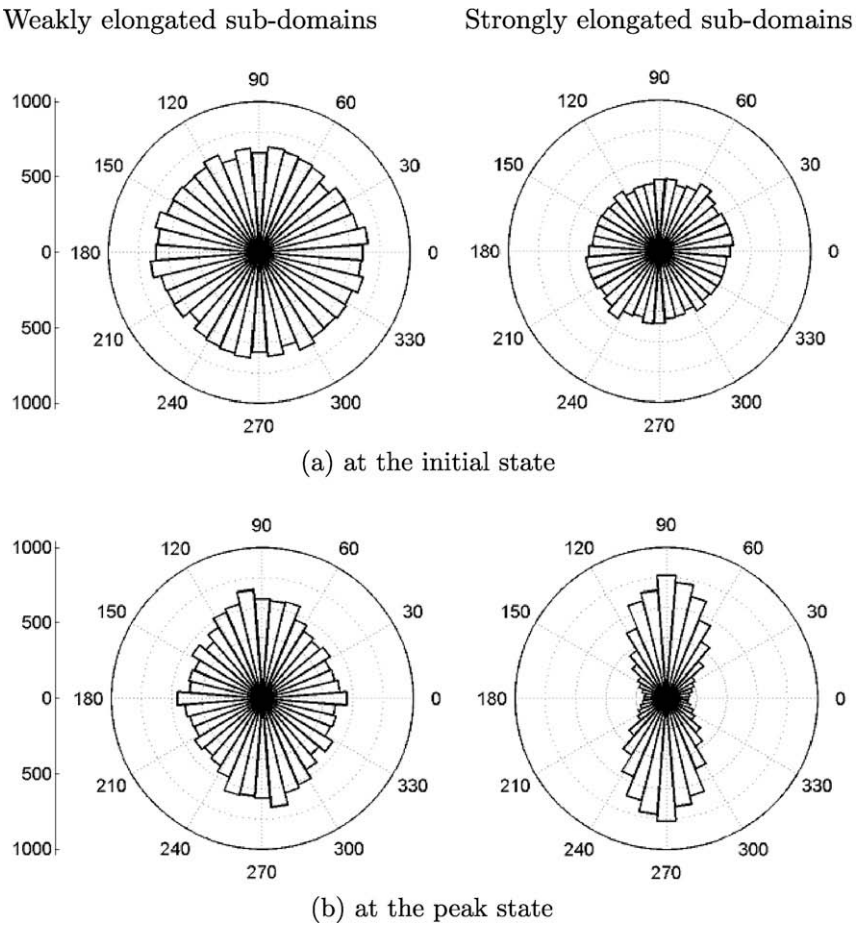

Fig. 11. Sub-domain distributions $N^h(\theta)$ for the two elongation classes at the initial and peak states.

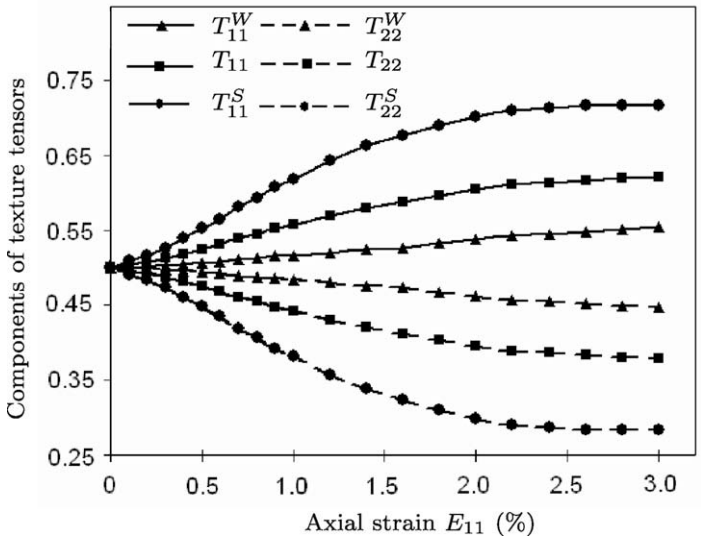

Fig. 12. Evolution of texture tensors $\boldsymbol{T}^S$, $\boldsymbol{T}$, $\boldsymbol{T}^W$ during loading.

each sub-domain. In the case of Kuhn's definition, the translation of the nodes is equal to the translation of the corresponding particle centers and the translation field is assumed to vary linearly along the edges of the sub-domains. The strain increment tensor of a sub-domain h, $\delta\boldsymbol{\varepsilon}^h$, is the symmetric part of the translation gradient tensor, $\delta\boldsymbol{a}^h$, which is derived from the relative translations between two centers of particles in its contacts by the following expression:

$$\delta\boldsymbol{a}^h = \frac{1}{6A^h} \sum_{j_1 j_2 \in \{0,1,\ldots,r^h-1\}} \boldsymbol{Q}^{r^h}_{j_1 j_2} \delta\boldsymbol{u}^{j_1} \otimes \boldsymbol{b}^{j_2} \tag{7}$$

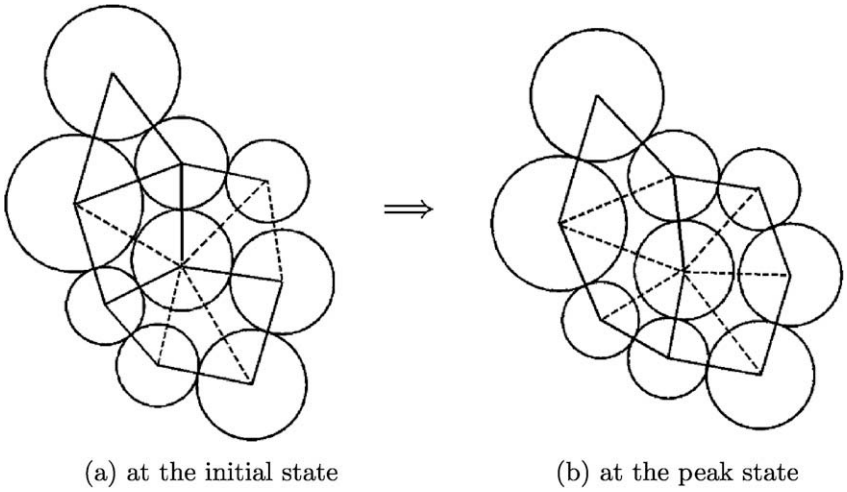

Fig. 13. Illustration of the formation of two new sub-domains in the major principal compression direction during the compression process.

Table 2
Characteristics of the six types of sub-domain at the initial state.

Characteristics	Types of sub-domain					
	WV	*WO*	*WH*	*SV*	*SO*	*SH*
Percentage by volume (%)	16.4	16.0	17.0	16.7	17.2	16.7
Percentage by number (%)	19.9	19.2	20.1	13.5	13.6	13.7
Mean elongation degree $\langle\beta^h\rangle_v$	0.11	0.11	0.11	0.29	0.29	0.29
Mean valence $\langle r^h\rangle$	3.58	3.58	3.63	4.56	4.57	4.51
Mean porosity $\langle\phi_1^h\rangle_v$	0.21	0.21	0.22	0.17	0.16	0.17
Mean porosity $\langle\phi_2^h\rangle_v$	0.16	0.16	0.16	0.16	0.16	0.16

where $\delta\boldsymbol{u}^{j_1}$ is the relative translation between two centers of particles in contact on edge j_1; $\boldsymbol{b}^{j_2}$ is an outward normal vector to edge j_2 with a magnitude equal to the length of edge j_2; $\boldsymbol{Q}^{r^h}_{j_1 j_2}$ is a skew symmetric and square matrix of dimension $r^h \times r^h$ which is defined in detail in Kuhn (1997, 1999); and A^h is the area of the sub-domain.

The mean strain tensor increment over all sub-domains can be computed as:

$$\delta\boldsymbol{E} = \frac{1}{A}\sum_{h=1}^{N} A^h \delta\boldsymbol{\varepsilon}^h \tag{8}$$

where A is the total area of all sub-domains taken into account in the particle graph.

In Table 4, the macroscopic strain increment tensor defined from the boundary condition is compared with that defined from relation (8) at two studied axial strain increments: $E_{11} = [0.2\%, 0.22\%]$ and $E_{11} = [1.2\%, 1.22\%]$. The two strain increment tensors are very similar. It should also be noted that the δE_{12} component derived from relation (8) is not zero but is very small compared to the δE_{11}, δE_{22} components. The slight difference between the values of $\delta\boldsymbol{E}$ derived from the two above-mentioned ways is due to the fact that the volume between the walls and the particle graph without the border sub-domains is not taken into account when computing $\delta\boldsymbol{E}$ from relation (8). A similar result was discussed by Bagi (2006).

Table 3
Characteristics of the six types of sub-domain at the peak state.

Characteristics	Types of sub-domain					
	WV	*WO*	*WH*	*SV*	*SO*	*SH*
Percentage by volume (%)	21.3	15.5	13.0	29.7	13.7	6.8
Percentage by number (%)	22.0	19.0	18.5	22.3	11.7	6.5
Mean elongation degree $\langle\beta^h\rangle_v$	0.13	0.12	0.11	0.31	0.30	0.29
Mean valence $\langle r^h\rangle$	4.10	3.83	3.61	5.11	4.80	4.48
Mean porosity $\langle\phi_1^h\rangle_v$	0.23	0.20	0.18	0.18	0.16	0.16
Mean porosity $\langle\phi_2^h\rangle_v$	0.16	0.15	0.15	0.15	0.15	0.15

4. Strain–structure relationship at the meso-scale

The relationship between the strain and the structure for granular materials at the macro-scale is well-known in the literature. An isotropic assembly deforms differently from an anisotropic one (Oda, 1972; Konishi et al., 1982). Moreover, for a given anisotropic assembly, the deformation of the assembly depends strongly on the loading direction (Cambou and Lanier, 1988). In this section, we investigate whether there is a similar relation between strain and structure at the meso-scale.

Four kinds of strain increment derived from the strain tensor increment $\delta\boldsymbol{\varepsilon}^h$ at the meso-scale are analyzed:

- Strain increment component in the major principal compression direction $\delta\varepsilon_{11}^h$ labeled *major strain increment* (Section 4.1).
- Strain increment component in the minor principal compression direction $\delta\varepsilon_{22}^h$ labeled *minor strain increment* (Section 4.2).
- *Volumetric strain increment* $\delta\varepsilon_v^h = \delta\varepsilon_{11}^h + \delta\varepsilon_{22}^h$ (Section 4.3).
- *Volume change* $\Delta V^h = \delta\varepsilon_v^h V^h$ (Section 4.4).

The relations shown hereafter are statistical relations, for which the volume-weighted average strain is computed for a set of sub-domains. The relationship between four kinds of strain increment $\delta\varepsilon_{11}^h$, $\delta\varepsilon_{22}^h$, $\delta\varepsilon_v^h$, ΔV^h and sub-domain orientation θ^h is represented by polar diagrams where sub-domains belonging to each elongation class are sorted, according to the value of θ^h, into 40 sets corresponding to 40 orientation angle intervals.

Table 4
Comparison of the strain increment tensors defined from the boundary condition and from relation (8).

$\delta\boldsymbol{E}$	Prescribed axial strain increment	
	$E_{11} = [0.2\%, 0.22\%]$	$E_{11} = [1.2\%, 1.22\%]$
By boundary condition	$\begin{bmatrix} 5.26\times10^{-5} & 0.0 \\ 0.0 & -2.00\times10^{-4} \end{bmatrix}$	$\begin{bmatrix} 2.20\times10^{-4} & 0.0 \\ 0.0 & -2.00\times10^{-4} \end{bmatrix}$
By relation (8)	$\begin{bmatrix} 5.20\times10^{-5} & 8.41\times10^{-7} \\ 8.41\times10^{-7} & -1.98\times10^{-4} \end{bmatrix}$	$\begin{bmatrix} 2.2\times10^{-4} & 2.69\times10^{-6} \\ 2.69\times10^{-6} & -1.99\times10^{-4} \end{bmatrix}$

The relationship between these kinds of strain increment and sub-domain orientation θ^h belonging to each elongation class will be investigated at two studied axial strain increments: $E_{11} = [0.2\%, 0.22\%]$ and $E_{11} = [1.2\%, 1.22\%]$ in the contractive and dilative zones of the macroscopic volumetric behavior, respectively. The dotted line in Figs. 14, 16 and 18 corresponds to the macroscopic strain of the granular assembly. Section 4.5 proposes some explanations for the relationship between strain and structure at the meso-scale. Finally, Section 4.6 discusses the role of the induced anisotropy of the assembly on the strain at the meso-scale.

4.1. Analysis of major strain increment $\delta\varepsilon_{11}^h$

The relationship between major strain increment $\delta\varepsilon_{11}^h$ and sub-domain orientation θ^h for the two elongation classes is shown in Fig. 14. A negative value of $\delta\varepsilon_{11}^h$ means that major strain increment $\delta\varepsilon_{11}^h$ is a compressive strain. Major strain increment $\delta\varepsilon_{11}^h$ is clearly heterogeneous and it depends significantly on sub-domain elongation degree β^h and on sub-domain orientation θ^h. *Major strain increment $\delta\varepsilon_{11}^h$ is larger within the sub-domains oriented in the minor principal compression direction than within the ones oriented in the major principal compression direction.* Moreover, major strain increment $\delta\varepsilon_{11}^h$ within the strongly elongated sub-domains depends significantly on sub-domain orientation θ^h, but this is not the case for the weakly elongated sub-domains.

The concentration of major strain increment $\delta\varepsilon_{11}^h$ within a sub-domain is quantified by a factor χ_{11}^h, called the *major strain concentration*, defined as the ratio between $\delta\varepsilon_{11}^h$ of the sub-domain and δE_{11} of the overall assembly ($\chi_{11}^h = \delta\varepsilon_{11}^h/\delta E_{11}$). A value of χ_{11}^h equal to 1.0 means that the sub-domain deforms in keeping with the macroscopic deformation in the major principal compression direction. Fig. 15 shows the evolution of the mean value of χ_{11}^h for the six types of sub-domain during loading. The value of χ_{11}^h for types *WH*, *SH* is higher than 1.0 while that for types *WO*, *SO*, *WV*, *SV* is lower than 1.0 throughout loading. This means that the sub-domains oriented in the minor principal compression direction deform more in the major principal compression direction than the overall assembly. The opposite is concluded for the sub-domains which are oriented obliquely and in the major principal compression direction. Of the six types of sub-domain, the value of χ_{11}^h for type *SH* is the highest and increases greatly during loading. Thus, we can conclude that *the strongly elongated sub-domains oriented in the minor principal compression direction play the most significant role in deformation at the meso-scale in the major principal compression direction.*

4.2. Analysis of minor strain increment $\delta\varepsilon_{22}^h$

Fig. 16 shows the relationship between minor strain increment $\delta\varepsilon_{22}^h$ and sub-domain orientation θ^h for the two elongation classes. A positive value of $\delta\varepsilon_{22}^h$ means that minor strain increment $\delta\varepsilon_{22}^h$ is an extensive strain. Unlike major strain increment $\delta\varepsilon_{11}^h$, *minor strain increment $\delta\varepsilon_{22}^h$ is greater within the sub-domains oriented in the major principal compression direction than that within the ones oriented in the minor principal compression direction.* Like to the $\delta\varepsilon_{11}^h$–θ^h relationship, the $\delta\varepsilon_{22}^h$–θ^h relationship is closely related to sub-domain elongation degree β^h: this is significant for the strongly elongated sub-domains but becomes much less significant for the weakly elongated ones.

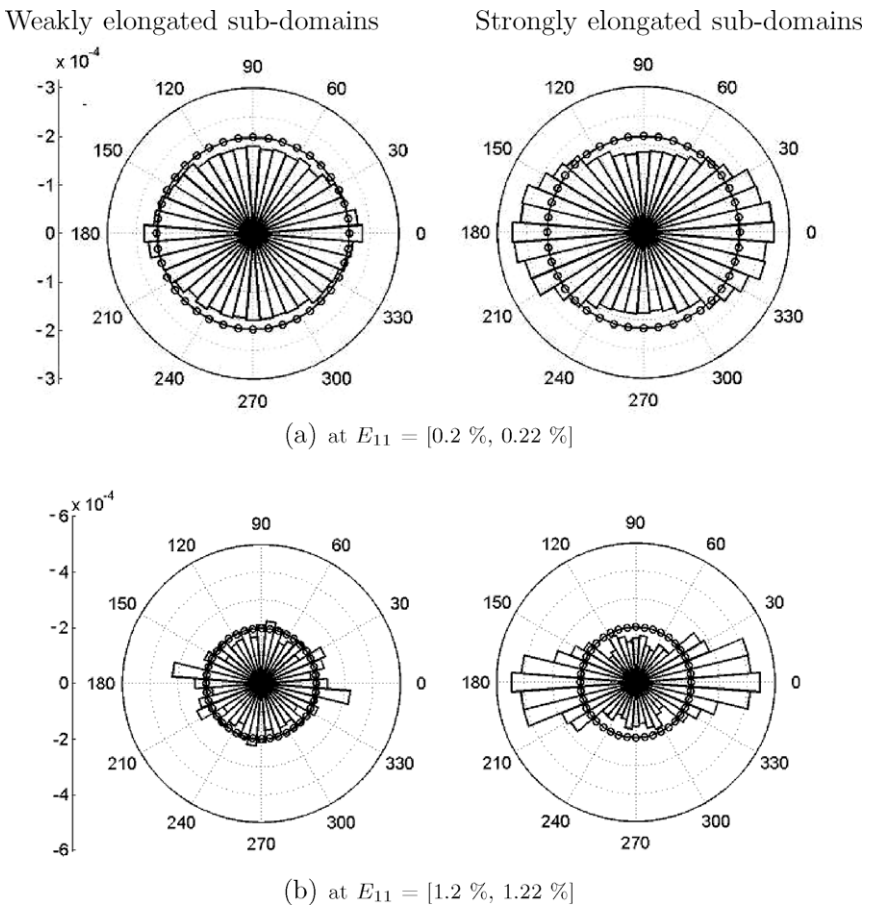

Fig. 14. Relationship between major strain increment $\delta\varepsilon_{11}^h$ and sub-domain orientation θ^h for the two elongation classes.

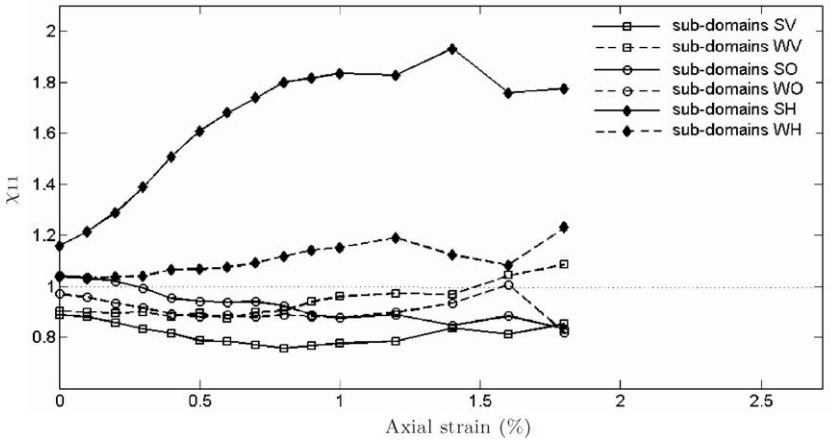

Fig. 15. Evolution of major strain concentration χ^h_{11} within the six types of sub-domain during loading.

The concentration of minor strain increment $\delta\varepsilon^h_{22}$ within a sub-domain is quantified by a factor χ^h_{22}, called the *minor strain concentration*, as the ratio between $\delta\varepsilon^h_{22}$ within the sub-domain and δE_{22} of the assembly ($\chi^h_{22} = \delta\varepsilon^h_{22}/\delta E_{22}$). The evolution of the mean value of χ_{22} for the six types of sub-domain during loading is shown in Fig. 17. Unlike major strain concentration χ^h_{11}, minor strain concentration χ^h_{22} for types *WV*, *SV* is higher than 1.0, while that for types *WH*, *SH*, *WO*, *SO* is lower than 1.0. This means that the sub-domains oriented in the major principal compression direction deform more in the minor principal compression direction than the overall assembly. The opposite is concluded for the sub-domains which are oriented obliquely and in the minor principal compression direction. Of the six types of sub-domain, minor strain concentration χ^h_{22} for type *SV* is the highest and increases greatly whereas that for type *SH* is the lowest and decreases significantly during loading. Thus, it could be concluded that *the strongly elongated sub-domains oriented in the major principal compression direction*

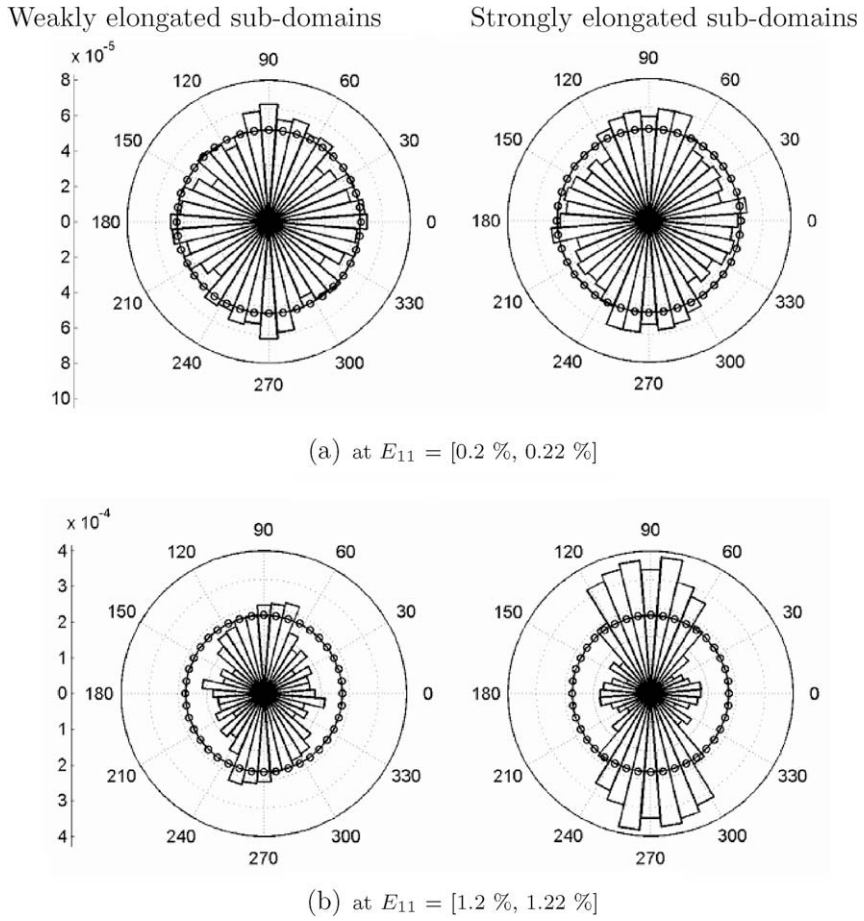

(a) at $E_{11} = [0.2\ \%, 0.22\ \%]$

(b) at $E_{11} = [1.2\ \%, 1.22\ \%]$

Fig. 16. Relationship between minor strain increment $\delta\varepsilon^h_{22}$ and sub-domain orientation θ^h for the two elongation classes.

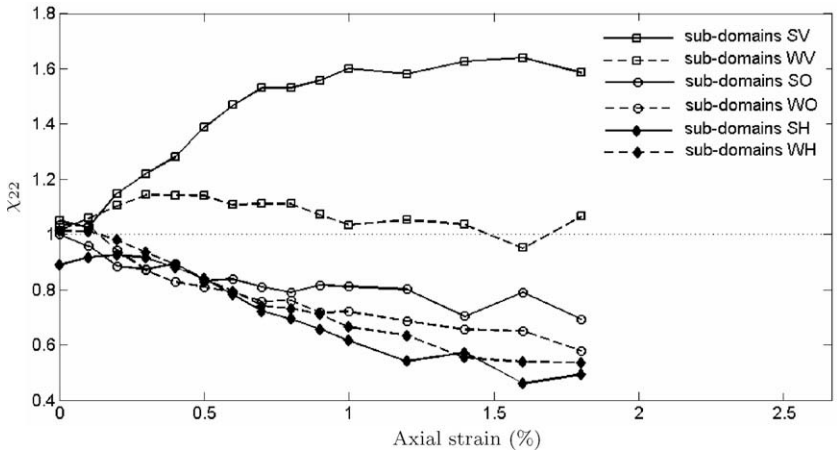

Fig. 17. Evolution of minor strain concentration χ^h_{22} within the six types of sub-domain during loading.

play the most important role in deformation at the meso-scale in the minor principal compression direction.

4.3. Analysis of volumetric strain increment $\delta\varepsilon^h_v$

Fig. 18 shows the relationship between volumetric strain increment $\delta\varepsilon^h_v$ and sub-domain orientation θ^h for the two elongation classes. The solid line and the dashed line correspond to the contractive and the dilative volumetric strains, respectively. At the early stage of the test when the overall assembly contracts, all sub-domains contract. *The sub-domains oriented in the minor principal compression direction contract more than those oriented in the major principal compression direction.* Moreover, volumetric strain increment $\delta\varepsilon^h_v$ within the strongly elongated sub-domains depends significantly on sub-domain orientation θ^h but a weak dependence is observed for the weakly elongated sub-domains.

When the granular assembly dilates, local dilative zones appear. *These dilative zones correspond to the sub-domains oriented in the major principal compression direction while local contractive zones correspond to the sub-domains oriented in the minor principal compression direction*, as shown in Fig. 18(b). This result is in good agreement with the one found out by Kuhn (1999). Furthermore, the volumet-

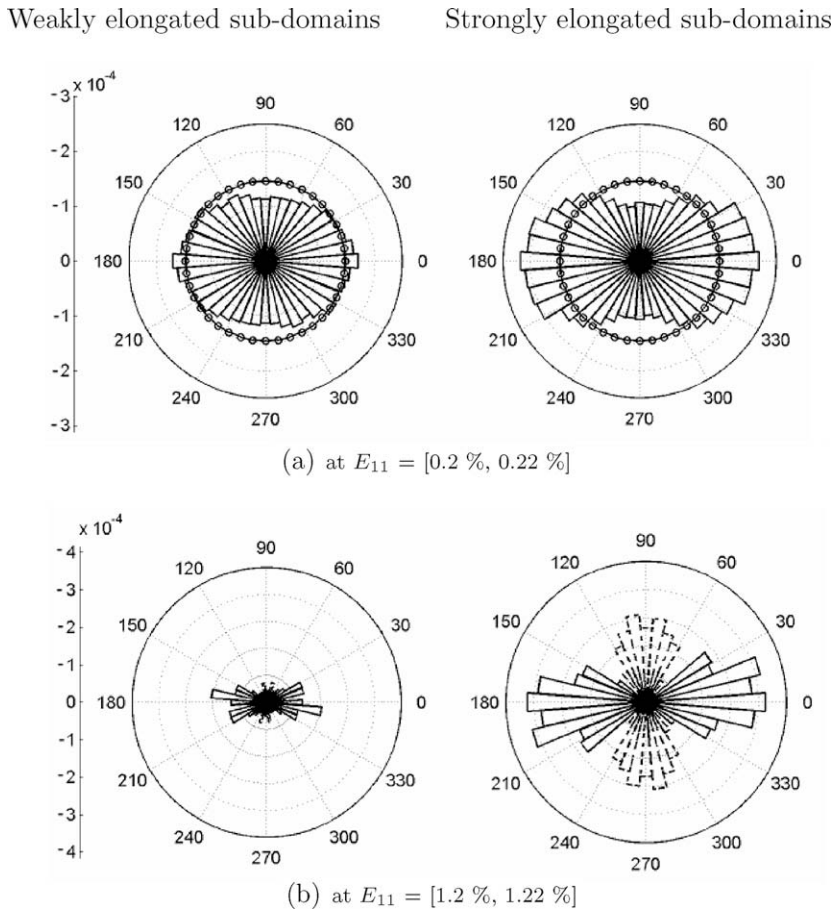

Fig. 18. Relationship between volumetric strain increment $\delta\varepsilon^h_v$ and sub-domain orientation θ^h for the two elongation classes.

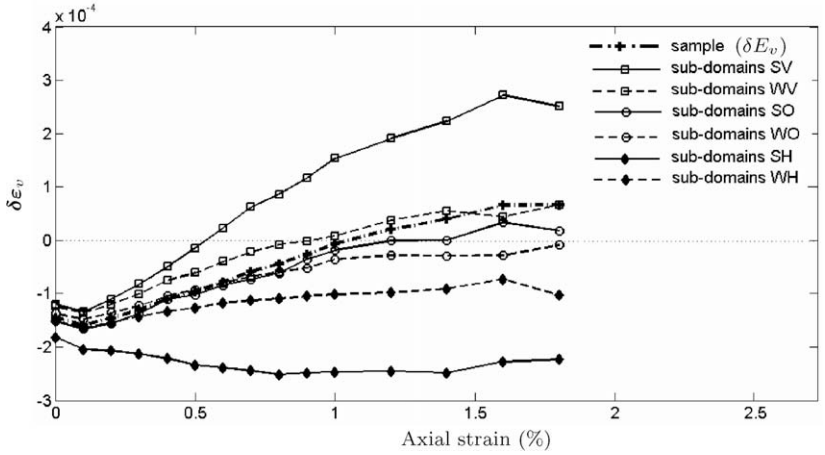

Fig. 19. Evolution of volumetric strain increment $\delta\varepsilon_v^h$ within the six types of sub-domain during loading.

ric behavior of the strongly elongated sub-domains is much more marked than that of the weakly elongated sub-domains.

The evolution of mean volumetric strain increment $\delta\varepsilon_v^h$ for the six types of sub-domain during loading, compared to macroscopic volumetric strain increment δE_v, is shown in Fig. 19. The value of $\delta\varepsilon_v^h$ for types *WV*, *SV* is higher than δE_v. The opposite is observed for types *WH*, *SH*. This means that the sub-domains oriented in the major principal compression direction are less contractive but more dilative than the overall assembly. The opposite is concluded for the sub-domains oriented in the minor principal compression direction. It can be noted that dilatancy takes place within type *SV* even when the overall granular sample still contracts. Of the six types of sub-domain, the volumetric behavior of types *SV*, *SH* is very different from that of the sample: type *SV* dilates more and more during loading whereas type *SH* invariably contracts. In conclusion, *the strongly elongated sub-domains play a dominant role in volumetric deformation at the meso-scale: contractancy takes place within the sub-domains oriented in the minor principal compression direction and dilatancy takes place within the sub-domains oriented in the major principal compression direction.*

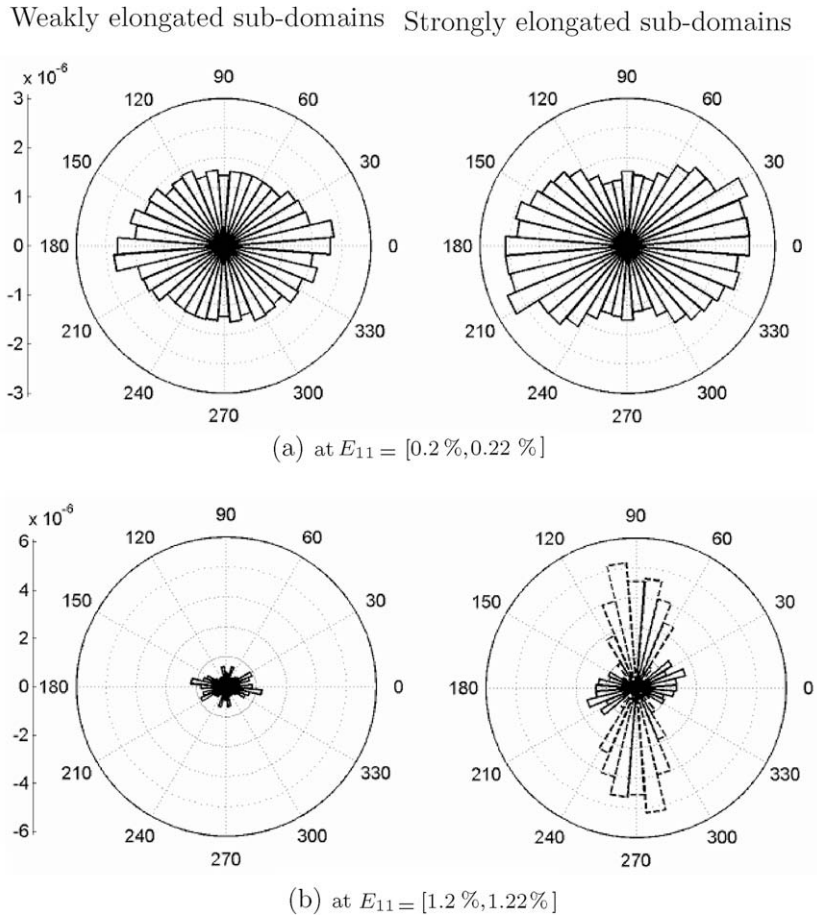

Fig. 20. Relationship between volume change ΔV^h and sub-domain orientation θ^h for the two elongation classes.

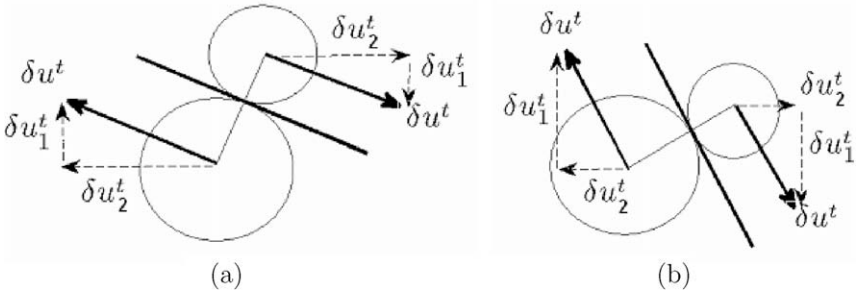

Fig. 21. Relative movements between two centers of particles in contact along contact sliding planes for two contacts oriented in the major (a) and minor (b) principal compression directions.

4.4. Analysis of volume change ΔV^h

The relationship between volume change ΔV^h and sub-domain orientation θ^h is shown in Fig. 20 which represents the total volume change (normalized by the volume of the assembly) of all sub-domains oriented in a given angle interval. At strain increment $E_{11} = [0.2\%, 0.22\%]$ where the sub-domain distribution remains fairly *isotropic*, the ΔV^h–θ^h relationship is approximately similar to the $\delta\varepsilon_v^h$–θ^h relationship shown in Fig. 18(a). However, at the strain increment $E_{11} = [1.2\%, 1.22\%]$ where the sub-domain distribution is strongly anisotropic, the ΔV^h–θ^h relationship is very different from the $\delta\varepsilon_v^h$–θ^h relationship. It can be seen that the strongly elongated sub-domains mainly contribute to the volume change of the overall assembly. Furthermore, the *volume increase* of the sub-domains oriented in the major principal direction is dominant with respect to the *volume decrease* of the sub-domains oriented in the minor principal compression direction. This result can be explained by the fact that, on one hand, the strongly elongated sub-domains tend to be oriented in the major principal compression direction and, on the other hand, the sub-domains oriented in the latter direction tend to dilate more and more during loading. Thus, it can be concluded that *the dilatancy of the overall sample is mainly due to the volume increase of the strongly elongated sub-domains oriented in the major principal compression direction.*

4.5. Explanations for the strain–structure relationship at the meso-scale

For granular materials whose particles are quasi-rigid, the relative movements between particles in contact are constrained along contact sliding planes, as shown in Fig. 21. As a consequence, the strain of a granular assembly is mainly due to, from a micromechanical point of view, the relative translations between two centers of particles in contact along contact sliding planes. This result was confirmed by Kruyt and Antony (2007).

In fact, contact sliding planes in an elongated sub-domain tend to be preferentially oriented in the elongation direction, as illustrated in Fig. 22 (the orientation of a plane defined as the orientation of its normal). Consequently, the relative translations between the particles in contact of a sub-domain oriented in the major (respectively, minor) principal compression direction take place preferentially in the minor (respectively, major) principal compression direction. This leads to a higher value of minor strain increment $\delta\varepsilon_{22}^h$ (respectively, major strain increment $\delta\varepsilon_{11}^h$) within the sub-domains oriented in the major (respectively, minor) principal compression direction. Nevertheless, the tendency of preferential contact orientation in the elongation direction of a weakly elongated sub-domain is weaker than that of a strongly elongated one. Consequently, the $\delta\varepsilon_{11}^h$–θ^h, $\delta\varepsilon_{22}^h$–θ^h relationship for the weakly elongated sub-domains is much weaker than for the strongly elongated ones.

4.6. Role of the induced anisotropy of the sample on the strain at the meso-scale

The evolution of the four kinds of strain increment $\delta\varepsilon_{11}^h$, $\delta\varepsilon_{22}^h$, $\delta\varepsilon_v^h$, ΔV^h within the sub-domains during the biaxial compression process as mentioned above, underlines the role of the induced anisotropy of the granular assembly during loading. Indeed, during the biaxial compression process, there is creation and loss of contacts in the major and minor principal compression directions, respectively. As a consequence, on one hand, sub-do-

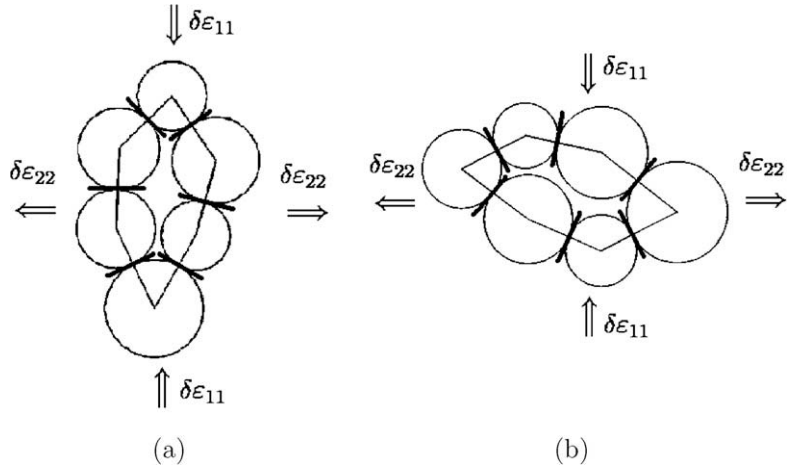

Fig. 22. Orientation of contact sliding planes in two sub-domains oriented in the major (a) and minor (b) principal compression directions.

mains lose the contacts which play a role in confining them in the minor principal compression direction resulting in loss of contacts in this direction. On the other hand, sub-domains are more compressed in the major principal compression direction, resulting in creation of contacts in this direction. Because compression loading increases in the major principal direction and confinement ability decreases in the minor principal compression direction, a sub-domain oriented in the major principal compression direction deforms more and more in the minor principal compression direction and dilates more and more during loading. These are also the reasons why a sub-domain oriented in the minor principal compression direction deforms more and more in the major principal compression direction during loading.

5. Conclusions

The meso-scale introduced in this paper, based on sub-domains surrounded by load-bearing particles, appears to be an appropriate scale to analyze the internal heterogeneity in terms of structure inside a granular material. The porosity without isolated particles and the valence of sub-domains are well correlated. The mesoscopic structure evolves greatly during the biaxial compression test, and this evolution is closely linked to the contact distribution in the granular assembly. In particular, the strongly elongated sub-domains tend to be much more oriented in the compression direction than the weakly elongated sub-domains.

Sub-domains do not deform in keeping with the overall assembly. Strain within sub-domains depends significantly on the sub-domain elongation degree and on the sub-domain orientation. Of the sub-domains, the strongly elongated sub-domains play a much more significant role in deformation at the meso-scale than the weakly elongated ones. Strain in the major (respectively, minor) principal compression direction is more concentrated within the strongly elongated sub-domains oriented in the minor (respectively, major) principal compression direction. In addition, contractancy takes place mostly within the strongly elongated sub-domains oriented in the minor principal compression direction while dilatancy takes place mostly within the strongly elongated ones oriented in the major principal compression direction.

The usual multi-scale approaches for kinematic variables which consider the micro-scale at contact level assume that the kinematics at a contact depend on contact orientation (Emeriault and Cambou, 1996; Kruyt and Rothenburg, 2004). The results exposed in this paper allow us to conclude that the kinematics at a contact depend not only on the orientation of this contact but also on the structure of the sub-domain containing this contact. Indeed, the relative translation between two centers of particles in a contact which is contained in a weakly elongated sub-domain is different from that in a contact with the same orientation but contained in a strongly elongated one, which results from the difference between strain within a weakly elongated sub-domain and that within a strongly elongated one.

During loading the mesoscopic strain evolves as well as the internal structure of the whole granular assembly. This evolution is attributed to the induced anisotropy of the granular assembly and closely related to the structure of the sub-domains. The concentration of strain in the major (respectively, minor) principal compression direction within the strongly elongated sub-domains oriented in the minor (respectively, major) principal compression direction is shown to increase greatly during the compression process. Moreover, the strongly elongated sub-domains oriented in the major principal compression direction tend to dilate more and more when the induced anisotropy of the whole granular assembly increases while the strongly elongated sub-domains oriented in the minor principal compression direction tend to invariably contract.

Once this appropriate meso-scale has been defined, future works will focus on the strain localization relation between the macro- and meso-scales (following for example the line developed in Emeriault and Cambou (1996), Emeriault and Chang (1997) and Magoariec et al. (2008)). Then, a consistent definition of stress within sub-domains will be defined and a relationship between the formerly defined strain, stress and structure at the meso-scale will be investigated with the *ambitious* goal of completing the homogenization process for granular materials.

References

Bagi, K., 1996. Stress and strain in granular assemblies. Mechanics of Materials 22, 165–177.

Bagi, K., 2006. Analysis of microstructural strain tensors for granular assemblies. International Journal of Solids and Structures 43, 3166–3184.

Cambou, B., Lanier, J., 1988. Induced anisotropy in cohesionless soils, experiments and modelling. Computers and Geotechnics 6, 291–311.

Cambou, B., Chaze, M., Dedecker, F., 2000. Change of scale in granular materials. European Journal of Mechanics A 19, 999–1014.

Cundall, P.A., 1971. A computer model for simulating progressive large scale movements in blocky rock systems. In: Proceedings of the Symposium of the International Society of Rock Mechanics, Nancy, France, vol. 1, Paper No. II-8.

Cundall, P.A., Strack, O.D., 1979. A discrete numerical model for granular assemblies. Geotechnique 29, 47–65.

Dedecker, F., Chaze, M., Dubujet, P., Cambou, B., 2000. Specific features of strain in granular materials. Mechanics of Cohesive-Frictional Materials 5, 173–193.

Emeriault, F., Cambou, B., 1996. Micromechanical modelling of anisotropy nonlinear elasticity of granular medium. International Journal of Solids and Structures 33 (18), 2591–2607.

Emeriault, F., Chang, C.S., 1997. Interparticle forces and displacements in granular materials. Computers and Geotechnics 20 (3/4), 223–244.

Guibas, L.J., Knuth, D.E., Sharir, M., 1990. Randomized incremental construction of Delaunay and Voronoi diagrams. Lecture Notes in Computer Science, vol. 443. Springer, New York, pp. 414–431.

Konishi, J., Oda, M., Nemat-Nasser, S., 1982. Inherent anisotropy and shear strength of assembly of oval cross-sectional rods. In: Vermeer, P., Luger, H. (Eds.), Deformation and Failure of Granular Materials. A.A. Balkema, Rotterdam, The Netherlands, pp. 403–412.

Kruyt, N.P., Antony, S.J., 2007. Force, relative-displacement, and work networks in granular materials subjected to quasi-static deformation. Physical Review E 75, 051308.

Kruyt, N.P., Rothenburg, L., 1996. Micromechanical definition of the strain tensor for granular materials. Journal of Applied Mechanics 118, 706–711.

Kruyt, N.P., Rothenburg, L., 2004. Kinematic and static assumptions for homogenization in micromechanics of granular materials. Mechanics of Materials 36 (12), 1157–1173.

Kuhn, M.R., 1997. Deformation measures for granular materials. In: Mechanics of Deformation and Flow of Particulate Materials Division of ASCE, pp. 91–104.

Kuhn, M.R., 1999. Structured deformation in granular materials. Mechanics of Materials 31, 407–429.

Kuhn, M.R., 2003. Heterogeneity and patterning in the quasi-static behavior of granular materials. Granular Matter 4, 155–166.

Lee, D.T., Schachter, B.J., 1980. Two algorithms for constructing the Delaunay triangulation. International Journal of Computer and Information Science 9 (3), 219–242.

Magoariec, H., Danescu, A., Cambou, B., 2008. Nonlocal orientation distribution of contact forces in granular sample containing elongated particles. Acta Geotechnica 3, 49–60.

Oda, M., 1972. Initial fabrics and their relations to mechanical properties of granular material. Soils and Found 12, 17–36.

Oda, M., Kazama, H., 1998. Microstructure of shear band and its relation to the mechanisms of dilatancy and failure of dense granular soils. Geotechnique 48 (1), 1–17.

Satake, M., 1992. A discrete-mechanical approach to granular materials. International Journal of Engineering Science 30 (10), 1525–1533.

Tsuchikura, T., Satake, M., 1998. Statistical measure tensors and their application to computer simulation analysis of biaxial compression test. In: Murakami, H., Luco, J.E. (Eds.), Engineering Mechanics: A Force for 21st Century. ASCE, Reston, VA, pp. 1732–1735.

Yoshida, T., Tatsuoka, F., Siddiquee, M.S.A., Kamegai, Y., Park, C.-S., 1994. Shear banding in sands observed in plane strain compression. In: Chambon, R., Desrues, J., Vardoulakis, I. (Eds.), Symposium on Localization and Bifurcation Theory for Soils and Rocks. Balkema, Amsterdam, pp. 165–179.